Monthly Notices of the ROYAL ASTRONOMICAL SOCIETY

MNRAS **538,** 867–874 (2025) https://doi.org/10.1093/mnras/staf249
Advance Access publication 2025 February 14

Pupil plane intensity interferometry with imaging air Cherenkov telescopes

N. Matthews [1,2★] P. M. Gori[3] and F. Vakili[3]

[1] *Institut de Physique de Nice, CNRS, Université Côte d'Azur, F-06200, Nice, France*
[2] *Space Dynamics Laboratory, Utah State University, Logan, UT, 84341, USA*
[3] *Université Côte d'Azur, Observatoire de la Côte d'Azur, CNRS, Laboratoire Lagrange, F-06304, Nice, France*

Accepted 2025 January 21. Received 2025 January 20; in original form 2024 August 5

ABSTRACT

The Intensity Interferometry Imaging Telescope (I3T) concept illustrated how a single imaging air Cherenkov telescope (IACT) can be transformed into a multi-element intensity interferometer. This is achieved by segmenting the light collecting surface into many sub-apertures via active control of individual mirror facets. Here, we propose an alternative method applicable to all IACTs that we refer to as pupil plane intensity interferometry. Principally, the re-imaged pupil of an IACT can be subdivided with a multipixel detector to enable extremely dense uv-plane sampling. Ray tracing of an IACT based on one of the Very Energetic Radiation Imaging Telescope Array System (VERITAS) light collectors was performed as a proof of principle. Several unique science cases could be investigated and, in particular, we performed a case study that indicates the ability to strongly constrain the angular brightness distribution of the extended disc of the Be star Gamma Cassiopeia. The proposed design could be used as an alternative to current intensity interferometry instruments as it mitigates several inherent limitations of IACTs when used as intensity interferometers, namely temporal dispersion and large angular point spread functions.

Key words: techniques: high angular resolution – techniques: interferometric – stars: atmospheres – stars: rotation.

1 INTRODUCTION

Interferometry of stellar targets at optical wavelengths is a powerful technique to obtain the spatial resolution needed to resolve a variety of astrophysical phenomena. For a given wavelength λ, the resolution of the interferometer is fixed by the largest separation or baseline B between light collecting elements extending resolution capabilities to $\sim\lambda/B$, far beyond what is possible using a single light collector. Conventional optical interferometry, herein referred to as direct interferometry, is performed by superimposing beams from separated telescopes to form interference fringes. The contrast of the fringes, or visibility, measures the target spatial mutual degree of coherence that is given by the Fourier transform of the angular brightness distribution (Labeyrie, Lipson & Nisenson 2006). Measuring the visibility over many baselines thus allows one to spatially characterize the target with high angular resolution capabilities.

Alternatively, intensity interferometry, based upon the Hanbury Brown and Twiss effect (Hanbury Brown & Twiss 1954, 1956), measures squared visibilities through correlations of starlight intensity fluctuations observed at separated telescopes. While the sensitivity of intensity interferometry is significantly less than that of direct interferometry, its implementation is generally more straightforward. There is greater tolerance to path length fluctuations enabling robustness against atmospheric turbulence and even for operation at short optical wavelengths, complementing existing direct interferometry facilities. Furthermore, this allows the use of large light collectors of low-optical quality such as Imaging Air Cherenkov Telescopes (IACTs) designed for ground-based gamma-ray astronomy (LeBohec & Holder 2006). In contrast to the beam-combining required in a direct interferometer, the measurement and correlation of intensities allow a straightforward scaling to many telescopes. For example, starlight intensities can be recorded locally at each telescope with correlations between the data from each telescope performed in post-processing.

There are a variety of modern experimental intensity interferometry efforts. Steady progress has been made using metre-class optical telescopes resulting in successful on-sky observations (Guerin et al. 2017, 2018; Rivet et al. 2020; de Almeida et al. 2022; Matthews et al. 2023). IACT observatories are now providing stellar angular diameter measurements with sub-milliarcsecond resolution at wavelengths in the B photometric band (Abeysekara et al. 2020; Acciari et al. 2020; Abe et al. 2024; Acharyya et al. 2024; Zmija et al. 2024). A realization, central to the ideas presented in this work, came from the concept of the Intensity Interferometry Imaging Telescope (I3T; Gori et al. 2021) that transforms a single IACT into a multiple element intensity interferometer by utilizing existing active mirror control hardware. Notably, the MAGIC observatory already demonstrated a proof of concept by enabling their mirror control software to direct arbitrary sub-apertures of the light collector to different detectors and observed changes in the measured coherence with the baseline (Cortina et al. 2022).

In this work, we present an extension of the I3T concept, herein described as Pupil Plane Intensity Interferometry (2P2I). First, a brief

★ E-mail: nolankmatthews@gmail.com

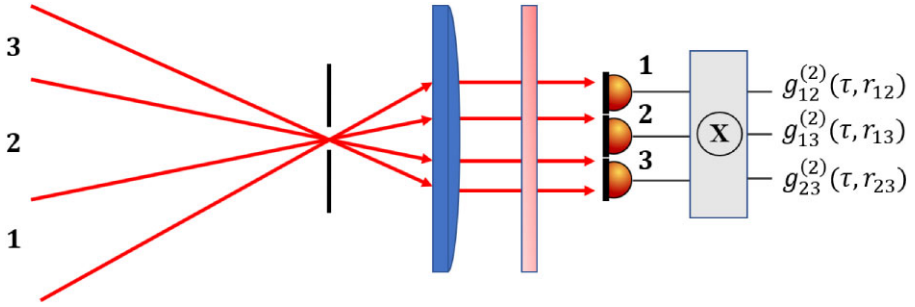

Figure 1. Illustration of the 2P2I technique. A field stop is placed at the focus of the telescope and the beam is subsequently collimated with a lens, passed through a narrowband spectral filter, and then sensed by a multipixel detector over the respective areas. Squared visibilities are calculated by measuring the normalized correlation function of detected light intensities $g^{(2)}$, measured between all detector pairs.

overview of the principles of intensity interferometry is presented in Section 2, and we then describe the 2P2I technique in Section 3. To validate its usefulness, a ray-tracing simulation of a proposed 2P2I design with an IACT-like telescope is performed and presented in Section 4. Using this design, a scientific case study of the ability to characterize the Hα envelope of Gam Cas is presented in Section 5. Finally, we conclude and provide some discussion in Section 6.

2 PRINCIPLES OF INTENSITY INTERFEROMETRY

Before introducing the concept of a pupil plane intensity interferometer, we first provide a general overview of the intensity interferometry technique. A two-element intensity interferometer measures the second-order correlation function

$$g^{(2)}(r, \tau) = \frac{\langle I_1(t) I_2(r, t+\tau)\rangle}{\langle I_1\rangle\langle I_2\rangle}, \tag{1}$$

where the brackets indicate an average over time t, I_1, and I_2 are the intensities collected at telescopes 1 and 2, r is the projected baseline, and τ is the time-lag between signals. For thermal/chaotic light, the second-order correlation function is related to the first-order correlation function $g^{(1)}$ by the Siegert relation[1] (Siegert 1943)

$$g^{(2)}(r, \tau) = 1 + |g^{(1)}(r, \tau)|^2, \tag{2}$$

where $g^{(1)}$ can in general be separated into its temporal and spatial components $g^{(1)}(r, \tau) = g^{(1)}(\tau)V(r)$. The temporal dependence is given by the Wiener–Khintchine theorem that relates the first-order correlation function in τ to the Fourier transform of the light spectral density expressed in frequency (Wiener 1930; Khintchine 1934). The spatial dependence $V(r)$, equivalent to the interferometric visibility, relates the first-order correlation function in r to the Fourier transform of the target angular brightness distribution via the van Cittert–Zernike theorem (Born & Wolf 1980). For non-circularly symmetric sources, such as that considered in this paper, it is noted that the visibility should be defined in terms of orthogonal spatial coordinates.

However, the coherence time τ_o in most practical situations is much less than the detector resolution time. The profile of the correlation function in τ is then determined instead by the timing response of the detectors. In this regime, the signal-to-noise ratio (S/N) of the squared visibility (Hanbury Brown 1974) is

$$\mathrm{S/N} = A\alpha\eta|V(r)|^2\sqrt{T\Delta f/2}, \tag{3}$$

[1]The Siegert relation was originally derived in the context of scattered radio signals. Its novel application to light was not developed until the time of Hanbury Brown and Twiss.

where $A = \sqrt{A_1 A_2}$ is the geometric mean of the collection areas of the two telescopes A_1 and A_2, α is the global efficiency of the system, η is the spectral flux density of the source expressed in units of ph s^{-1} m^{-2} Hz^{-1}, T is the integration time, and Δf is the electronic bandwidth of the system that can be related to the time-resolution $\Delta t = (\Delta f/2)^{-1}$ via the Nyquist sampling theorem. Alternatively, the expression for the S/N can be derived, originally by Hanbury Brown & Twiss (1958) and reformulated in Wentz & Saha (2015), for the case of a coincidence counting, or photon time-tagging set-up as

$$\mathrm{S/N} = (N_1 N_2)^{\frac{1}{2}}\tau_o|V(r)|^2\sqrt{T/\Delta t}, \tag{4}$$

where N_1 and N_2 are the photon rates corresponding to linearly polarized light recorded in each of the detectors, given by $N_i = \int A_i\alpha\eta(\nu)\mathrm{d}\nu$, and τ_o is the coherence time of the light defined by

$$\tau_o = \int |g^{(1)}(\tau)|^2 d\tau = \int |s(\nu)|^2 \mathrm{d}\nu. \tag{5}$$

where $s(\nu)$ is the light spectral density at frequency ν (Mandel & Wolf 1995). For the subsequent sections in this paper, the equations above allow us to determine the expected signal-to-noise ratio of the pupil plane intensity interferometer given the experimental observables.

3 PUPIL PLANE INTENSITY INTERFEROMETRY

2P2I aims to subdivide the primary collecting surface of the telescope into many sub-apertures by placing a multipixel camera in the exit pupil plane of the telescope. This concept is illustrated in Fig. 1. Each 'pixel' samples some region of the light collector, where the mapping between the detection area and the sub-aperture region is determined by the optical system. By performing the intensity correlations between all possible pairs of detector outputs, the telescope is transformed into a multi-element intensity interferometer with $N(N-1)/2$ simultaneous baselines where N is the number of sub-divisions of the primary collecting surface. Effectively, this technique can be viewed as a somewhat analogous method of aperture-masking interferometery (Baldwin et al. 1986; Monnier, Tuthill & Danchi 1999), but without any masking of the light collector in the sense that the full area of the mirror is used, and to use intensity correlations as the method for retrieving squared visibilities instead of fringe visibilities measured through $g^{(1)}$. We note that this idea was previously considered for optical telescopes where the coupling from the pupil plane to the detectors, perhaps through a fibre-fed instrument, is generally more straightforward due to the significantly better optical quality (Dravins et al. 2005).

The idea of 2P2I was inspired by the I3T concept (Gori et al. 2021) as both techniques aim to segment the light collecting surface of IACTs into sub-apertures. The I3T concept proposes using actuators to direct each of the individual mirror facets of the light collector to different detectors whereas the 2P2I technique performs the segmentation in the pupil plane. The main advantage of the I3T method is that it is likely simpler to implement as it utilizes existing hardware of the telescopes. However, there are several unique advantages to the 2P2I approach that warrant a deeper investigation into its potential application.

In both approaches a given detector will measure a stellar target intensity of $\sim I_\star/N$, where $I_\star$ is the stellar intensity incident over the entire light collector. In the case of I3T, a given detector will sense the background light accumulated over the entire mirror area such that the background light intensity in each detector is fixed at $I_{\rm bkg}$. Therefore the ratio between the starlight to background intensity goes as $\sim I_\star/I_{\rm bkg}N$. Due to the large point spread function (PSF) of an IACT telescope, the light intensity from the background can be an appreciable fraction of the expected stellar intensity even for bright targets (Rou et al. 2013) and will be problematic when scaling to large N or to dim targets. However, for 2P2I the use of a field-stop at the primary focus fixes the starlight-to-background intensity ratio independently from the number of sub-apertures N, enabling a more straightforward scaling to a large number of sub-apertures.

There are several shared benefits to both the 2P2I and the I3T segmented aperture approach over standard 'single-pixel' methods currently being used with IACT telescopes. In regards to sensitivity, the inherent anisochronicity of some IACTs limits the achievable time resolution to that of the induced dispersion. This is attributed to a geometric effect from the positioning of the mirror facets of the light collector that are laid along parabolic or spherical surfaces. In the case of parabolic designs, the effect is less than hundreds of picoseconds, whereas for the Davies–Cotton design (Davies & Cotton 1957), in which the mirror facets are laid upon a sphere centred on the focal point, the temporal dispersion is of order a few nanoseconds. Both 2P2I and I3T techniques rely on detecting the light over sub-apertures over which the corresponding temporal dispersion is less than the full mirror area. Therefore, higher time resolution detection is possible to improve the sensitivity.

Finally, the 2P2I concept can be performed with any IACT. The I3T technique assumes the use of actively controlled mirror facets which are not available on all IACTs. Pupil plane subdivision can be implemented entirely with passive elements, albeit requires external hardware.

4 RAY-TRACING SIMULATIONS

The mapping between the rays that fall within a given region in the exit pupil plane and the collecting surface is made non-trivial as a result of the low-optical quality of IACTs. Thus, to evaluate the feasibility of the 2P2I concept we performed ray-tracing simulations using a model roughly based upon one of the VERITAS IACTs. Several physical effects are incorporated in these simulations which include the individual facet characteristics, telescope geometry, facet locations, and obstruction from the telescope camera and supporting structure. The simulations heavily rely on libraries of a ROOT-based simulator for ray-tracing (ROBAST), an open-source tool used widely for evaluating the performance of various IACT observatories (Okumura, Noda & Rulten 2016). The simulation of the full optical performance of the proposed 2P2I system proceeds in several incremental stages. Section 4.1 first describes the construction and ray-tracing simulation of the model telescope. A proposed 2P2I instrument is constructed in the software and described in Section 4.2. Finally, we characterize various performance metrics of the instrument in Section 4.3 under two schemes of the exit pupil subdivision.

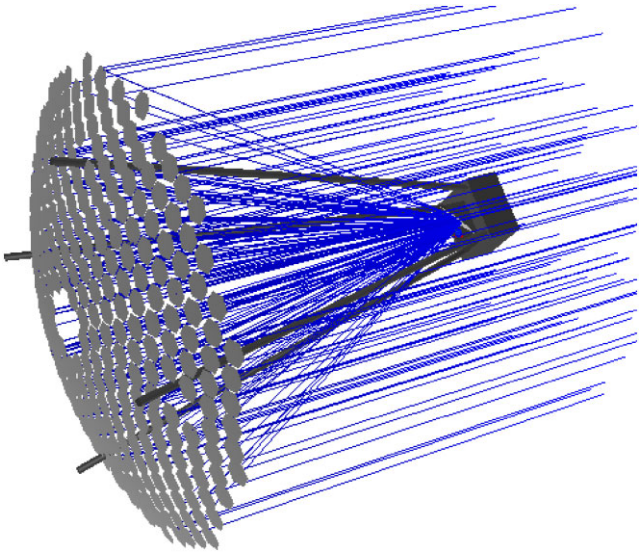

Figure 2. Image of the VERITAS-like telescope model constructed using ROBAST to evaluate the feasibility of the 2P2I concept. A random array of rays shown by the blue lines are thrown at the model telescope and propagated through the optical system.

4.1 Simulating the IACT

The geometry of the model telescope was taken from the VERITAS telescopes (Holder et al. 2006) which are based upon the Davies–Cotton optical design (Davies & Cotton 1957). The model is constructed by tiling all of the hexagonal facets along a sphere with a 12 m radius of curvature. Each facet has a flat to flat width of ∼61 cm and with a nominal radius of curvature of 24 m. The camera box that hosts the gamma-ray camera is created by inserting an obscuring rectangular element with dimension of 1.8 m × 1.8 m length by width and height of 1.4 m. Telescope arms are incorporated by four cylindrical beams with a diameter of 20 cm. Using this geometry a uniformly distributed parallel array of rays is thrown at the telescope model to simulate the telescope response to an object located on axis. An image of the telescope geometry as constructed using ROBAST is shown in Fig. 2.

Various aberrations and imperfections were incorporated into the ray-tracing model to closely match the performance of a real VERITAS telescope. Each mirror facet has an intrinsic finite spot size at its focus that was measured between 2 and 10 mm, with an average of 6.0 ± 0.5 mm defined by the 90 per cent containment diameter (Roache et al. 2008). Here, we simulate this by first scattering the light reflected of a given mirror facet away from the nominal Fresnel reflection by a random angle sampled from a Gaussian distribution. Here, the full width at half-maximum (FWHM) scattering angle used was 0.04° which corresponds to a FWHM spot size of 8 mm. Next, the nominal radius of curvature of each facet is 24 m, however, this value has RMS fluctuations of approximately 1 per cent over all facets. To incorporate this, the radius of curvature of each facet is a randomly sampled value from a Gaussian distribution centred at 24 m with an RMS width of 0.24 m (1 per cent). Finally, various facets were removed from the light collector based on a map of the

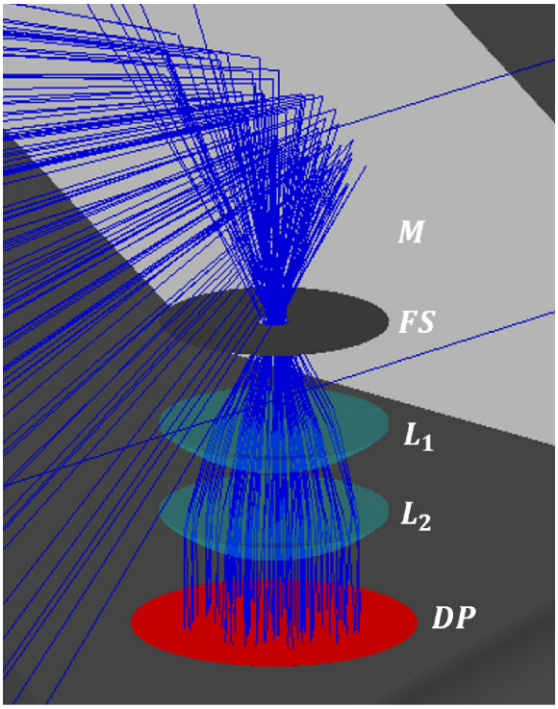

Figure 3. Image of the proposed 2P2I instrument as constructed using ROBAST. A 45-degree mirror (M) redirects the converging beam of the telescope on to a field stop (FS) located at the telescope's prime focus. The expanding beam is then collimated by two lenses (L_1 and L_2). Finally, the light is incident on to the detection plane (DP) which consists of a multipixel detector subdivided over the full area of the incident light. Not pictured is the necessary narrow-band spectral and optional polarization filter that would be naturally placed in the collimated beam between L_2 and DP.

VERITAS-T1 mirror facet location provided to us by the VERITAS collaboration. These missing facets correspond to the location of various calibration instrumentation mounted on the optical support structure of the telescope, and in the central region which is mostly obscured by the camera box.

The final evaluation of the telescope model was performed by characterizing the containment fraction of rays at the primary focus of the telescope. We find an 80 per cent containment diameter for angular PSF of 0.062° reasonably well-matched to on-sky measurements of the VERITAS PSF. Finally, we note these characterizations based on the VERITAS telescope should not be used as a reference for the performance of VERITAS, for example, in gamma-ray observations. Our goal was to reasonably approximate the optical response to serve as a proof-of-principle for the 2P2I concept.

4.2 Proposed elements of a 2P2I set-up

Following the construction of the model IACT, we add several optical elements near the telescope prime focus to enable its use as a multi-element interferometer. An image of the instrumentation as constructed using ROBAST is depicted in Fig. 3. A right-angle mirror is placed in front of the location of the gamma-ray camera to redirect the converging beam to the 2P2I instrument. A field stop, created by a thin cylinder with an open aperture of 25.4 mm diameter, is placed at the telescope's prime focus to limit the field of view. For the telescopes focal length of 12 m the open aperture corresponds to an angular field of view of ∼0.12° which is intentionally slightly larger than the telescope PSF to maximize the stellar light reaching the detector but reject off-axis background light.

The expanding beam after the focus is roughly collimated by a series of two identical lenses based on commercially available products.[2] Each lens is 200 mm in diameter with an effective focal length of 300 mm. The lenses are set in ROBAST as an *ALens* object with an index of refraction of 1.52 and constructed with the *TGeo* class of ROOT with a geometry following a spherical singlet lens. The spacing between the lenses is arbitrarily chosen to 80 mm. The separation from the prime focus was chosen by iterating over several values and examining the resulting angular distribution of the collimated beam after the second lens. We find a reasonable optimum by maximizing for parallel rays achieved at a 95 mm separation.

The 'detection plane', located at the intended location of the 2P2I camera, is placed in the collimated beam and records the transverse position of each ray. In addition, the entire path history is stored, corresponding to all vectors from world entry to the detection plane, including mirror reflections and lens interactions. This allows for the mapping of a given ray throughout the optical system and to be examined against various performance metrics.

4.3 Subdivision of the output pupil

The final stage of the 2P2I concept is to subdivide the detection plane utilizing a multipixel detector, possibly in conjunction with some concentrating optics such as lenses or Winston cones. In this study, we examined two tiling patterns corresponding to hexagonal and polar geometries. For the hexagonal tiling, 61 detectors or subdivisions were considered, where each hexagon has a flat to flat diameter of 21 mm. For the polar tiling, we consider eight radial and angular subdivisions each and are spaced radially such that each subdivision has approximately the same area. The rays that fall into each subdivision are then mapped back to the primary light collector from the ray-tracing history, which gives the effective area of each interferometer element. The partitioning of the exit pupil and mapping to the light collector is shown in Fig. 4 for both tilings, where the different colours represent the detection areas.

The angular and timing distributions of the rays in this subdivided scheme were examined and are shown in Fig. 5. The angular distribution of the rays over the entire collimated beam is compared against the distribution at the telescope focus. The collimating lenses provide a considerable improvement in the angular dispersion, bringing most rays to within a 7° angle with respect to the optical axis, in comparison to the f/1 beam of the telescope that extends to ∼26.6°. The distribution in the arrival time of photons over the entire light collector is spread over a ∼5.4 ns window. However, the arrival time distribution within a given sub-division can be considerably less than over the entire light collector. The exact distribution varies, and what is relevant is to compare the collected ensemble. In practice, when correlating between different subdivisions, each recorded time series can be shifted with respect to one another. The cumulative arrival time over all subdivisions is computed, where before accumulating, each time distribution is shifted so that the peak number of events occur at the same time lag. The result is shown in Fig. 5 demonstrating a strongly peaked distribution for both subdivisions with a slight improvement in the case of the polar tiling.

[2] http://catalog.rossoptical.com/catalog/large-optics/

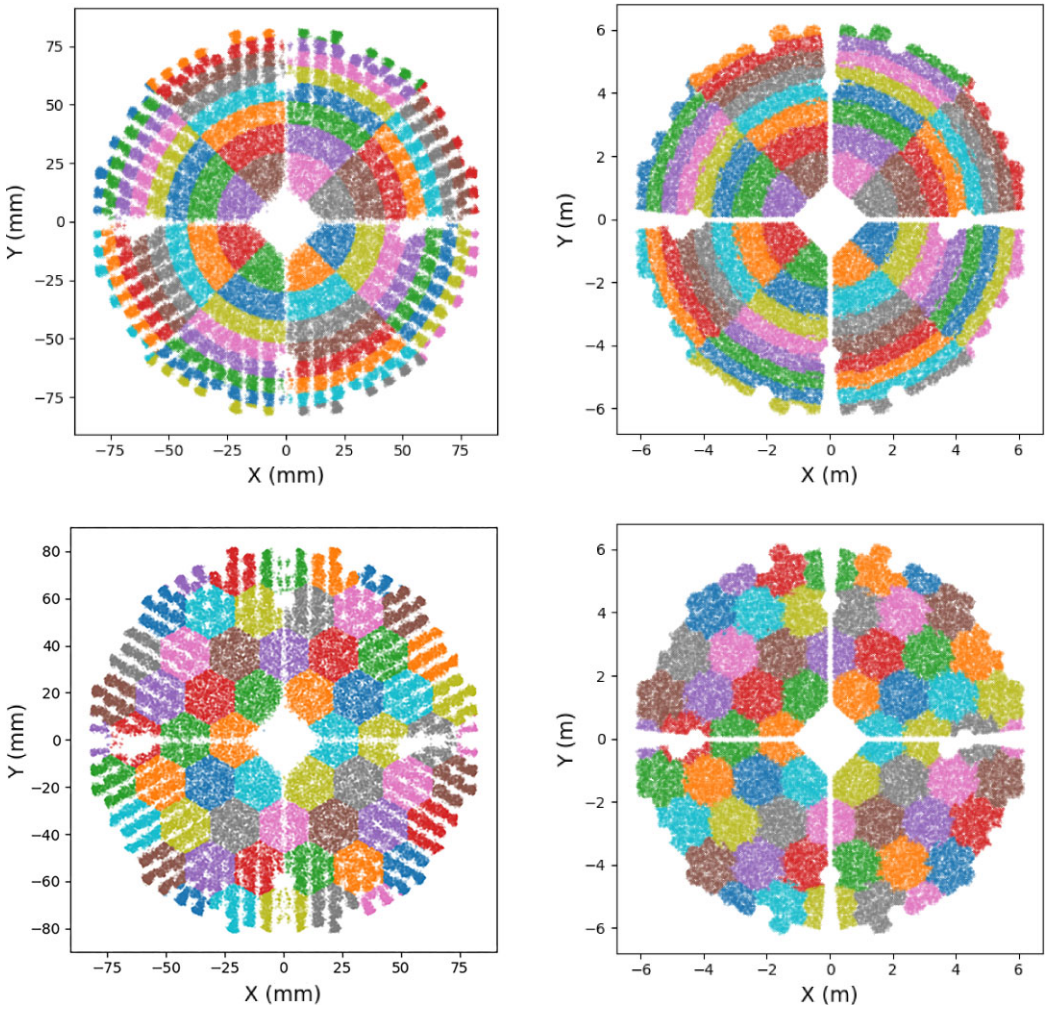

Figure 4. Mapping of rays from the subdivided re-imaged pupil (left) and the primary light collecting surface (right) in the case of a polar (top) and hexagonal tiling (bottom). Each colour indicates a different independent detection area subdivided over the pupil. The images on the right can be viewed as an array of individual 'telescopes', each given by a coloured region, that form the light collecting elements of an intensity interferometer.

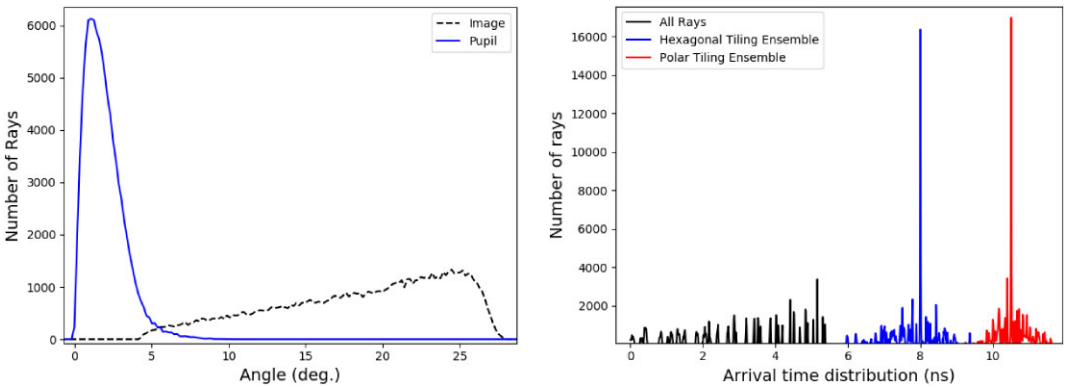

Figure 5. The left image shows the angular distribution of rays at the telescope primary focus in the dotted-black line to those in the simulated collimated beam in the solid blue. The right image shows the arrival time distribution of rays across the entire light collector (black, left-most) and the ensemble of sub-apertures for both the hexagonal (blue, center) and polar (red, right-most) tilings that are each shifted respectively to coincide the time-lag with the maximum number of photons. For clarity, the hexagonal and polar time distributions are shifted by an arbitrary delay.

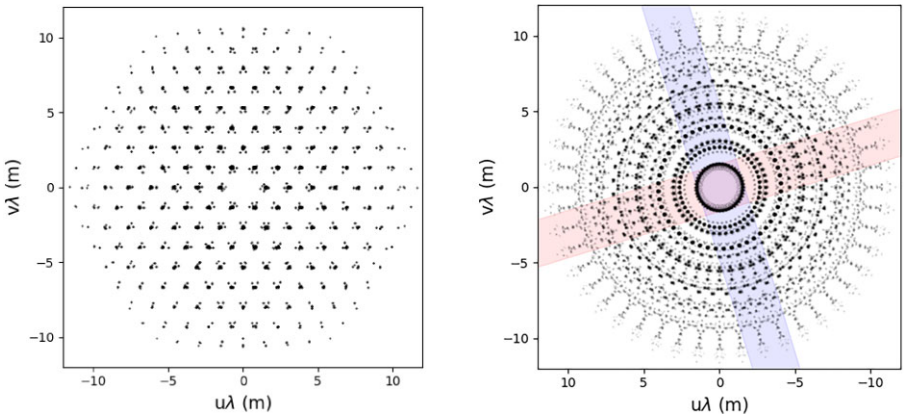

Figure 6. The left image shows the instantaneous uv-plane coverage at an hour angle of $h = 0$ for the hexagonal tiling implementation. The right image shows the total uv-plane coverage sampled at 30-min intervals for an observation of duration 8 h centred at $h = 0$. The coloured bands are aligned along the major and minor axis of the Gas Cas disc and the points within these bands are used to later illustrate the capability of resolving the elongation as shown in Fig. 7.

5 APPLICATIONS

5.1 A case study on the H α envelope of Gam Cas

To evaluate the scientific merit of the 2P2I concept, as a case study, we evaluate the ability to reconstruct the geometrical properties of the extended disc of the prototypical Be star Gam Cas using the set-up proposed in Section 4.2. Gam Cas is an interesting object that is widely studied because of its brightness and dynamic characteristics, which are observable over a wide range of the electromagnetic spectrum. In particular, optical interferometry has been employed several times by various observatories which primarily aim to characterize the brightness distribution of the extended disc observed in its H α emission. While the expected distribution of gas in the disc is non-trivial, interpretations of interferometric data generally employ a parametric model, typically an elongated Gaussian disc, to constrain various properties such as the disc extent, position angle, and axial ratio. Under these simplified assumptions, we explore the capability of the 2P2I concept to further constrain these measurements.

The simulated observation of Gam Cas is carried out as follows. We consider a single night observation of 8-h duration that takes place ± 4 h from a meridian transit in which the correlations are integrated over consecutive 30 min periods. The integration period is chosen to be long enough that a significant signal can be measured, but not so long that it samples over a large region of the uv-plane. To compute the uv-plane coverage, we use the hexagonal tiling scheme and approximate each subdivision as a point-like aperture, whose centres are defined by the centroid of the rays that fall into the respective subdivision, as depicted in Fig. 4. From these points, we compute the corresponding baseline separations along the horizontal and vertical axes along the light collector for all possible mirror facet pair permutations. The sampled points in the uv-plane are computed from these separation vectors taking into account the changing parallactic angle.

The instantaneous and total uv-plane sampling for these simulated observations are shown in Fig. 6. The instantaneous sampling corresponds to the uv-plane coverage at $h = 0$ that extends from the smallest separations of $\sim$1.5 m to just under the full diameter of the mirror at $\sim$11.7 m. For the 61 divisions proposed, the total number of sampled baselines is 1830 in a given snapshot or integration. For the entire simulated observation, there are 16 snapshots that in total provide 29 280 independent measurements of the squared visibility.

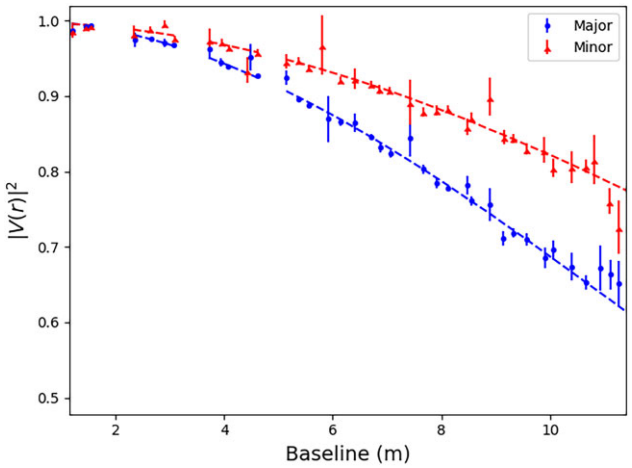

Figure 7. Simulated measurements of the elongated disc of Gam Cas using the proposed 2P2I instrument. The red and blue points represent the measurements of the squared visibility along the minor and major axes, respectively, obtained by a weighted mean of the sampled uv-plane points within the coloured bands shown in Fig. 6.

Notably, there is a higher density of sampling at shorter baselines due to redundancies resulting from the pupil plane subdivision. However, these points are not perfectly redundant due to imperfect optics and obstructing elements of the telescope. In practice, one may co-add points that are sufficiently close to improve the signal-to-noise at a given uv-plane position.

The angular brightness distribution of Gam Cas is modelled by an elongated Gaussian. We use the reported values from spectro-interferometric measurements from CHARA performed across the H α emission line that gives the FWHM extent as $\theta_{\rm GD} = 4.4$ mas, axial ratio of $r = 0.74$, and a position angle of 17° (Stee et al. 2012). Using equation (4) an uncertainty is assigned to each sampled point. For instrumental parameters, we assume a time-resolution of $\Delta t_{\rm r} = 2$ ns, efficiency of $\alpha = 10$ per cent, and integration time of $T = 30$ min. Using spectra from the Polarbase data base (Donati et al. 1997; Petit et al. 2014) taken on Gam Cas we estimate the expected photon rate and coherence time. The photon rate is obtained by first converting the normalized spectra from the data base into units of spectral flux density (ph s^{-1} m^2 Hz^{-1}). To accomplish this we first estimate the continuum flux $\eta_{\rm c} = \eta_0 \times 10^{(\Delta m_c/2.5)}$

where η_0 is the spectral flux density for a $R = 0$ magnitude star $\sim 1.0 \times 10^{-4}$ ph s^{-1} m^2 Hz^{-1} at 656.3 nm (Bessell 1979) and Δm_c is the magnitude of the continuum emission. The quoted value of the R-band magnitude for Gam Cas is 2.32, however, this includes the contribution of the emission line which we estimate to contribute $\sim$12 per cent over the integrated flux in the R band. The corrected magnitude for the continuum is then estimated at $m_c = 2.46$ which allows us to calculate the spectral flux density across the Hα line. For a spectral filter of bandpass $\Delta\lambda = 4$ nm centred on the Hα line, we calculate the expected measured photon rates over each subdivision taking into account the variation in the area. From the spectrum and equation (5), we calculate a coherence time of $\tau_o = 445$ fs. Finally, the photon rate in each subdivision is obtained taking into account the respective collection areas. For a characteristic sub-division, the area is $\sim$1.92 m^2 which for the calculated flux density and efficiency corresponds to a count rate of 86.9 Mcps in a given polarization mode. For this rate, and using the numbers above, we find an estimated signal-to-noise ratio of 36.7σ, or equivalently an uncertainty in the squared visibility of $\sigma_{V^2} = 0.027$, in the 30 min integration time assuming an unresolved $|V(r)|^2 = 1$ source.

Each sampled visibility in the uv-plane corresponds to the expected value from the elongated Gaussian disc model plus a random value sampled from a Gaussian distribution with an RMS width equal to the expected noise for that respective sample. The noise is approximated using equation (4) with the parameters already discussed. All sampled points and uncertainties are collected and we fit the elongated Gaussian disc model to the simulated data using the SCIPY least square minimization package OPTIMIZE.CURVE_FIT function. Fig. 7 shows averaged squared visibility measurements along the major and minor axes, obtained by points within the coloured bands in Fig. 6, illustrating the ability to resolve the disc elongation. The fit results return an expected uncertainty of 0.2 per cent in the disc extent, 0.5 per cent in the axial ratio, and 2 per cent in the position angle. Notably, these measurements would provide the strongest constraints on the geometrical parameters of the Gam Cas envelope to date. Continuous monitoring could potentially reveal and be used to characterize variations of the disc emission over time that follow changes in the variable emission line. Furthermore, one could search for deviations of the disc brightness distribution beyond a simple elongated Gaussian disc model.

5.2 Cool stellar types

Hanbury Brown and Twiss noted that there was a fundamental limit in how large a telescope could be made to improve the signal-to-noise for intensity interferometry observations, as at a certain size the target becomes fully resolved within a baseline corresponding to the telescope diameter (Hanbury Brown & Twiss 1958). Naturally, since at that time very large telescopes were necessary for a reasonable SNR, the most suitable targets were very hot stellar systems typically of the O, B, and A stellar types that were sufficiently bright and small. For IACT arrays, the shortest distance between telescopes is approximately 80 m and this imposes an upper limit on the practical observable target angular diameter. For example, a target with an angular diameter of 2 mas would be fully resolved at baselines greater than 60 m when observing at visual wavelengths. While shorter projected baselines can be obtained depending on the target sky position and array geometry, this requires observations at a high zenith angle, and the analysis is further complicated by the fact that a single telescope would partially resolve the target. However, pupil subdivision approaches like I3T or 2P2I enable short baselines with very large telescopes. While the sensitivity between a given pair of sub-apertures is reduced by the smaller collection area, it is partially compensated by the number of other pairs that sample a similar baseline. As a result, cooler stellar targets of larger angular diameter are observable thus overcoming limitations on the observable angular size and temperature for a given telescope size. Using the JMMC catalogue (Bourges et al. 2016), we find 186 potential targets with angular diameters between 2 and 15 mas, and a V-band magnitude less than 4 comprising stellar classifications ranging from B-type to M-type stars. Surveys of angular diameter measurements at short visible wavelengths would uniquely complement past (e.g. Challouf et al. 2014; Nardetto et al. 2020) and planned (Mourard et al. 2022) efforts towards calibration of the surface brightness colour relation. Alternatively, these approaches could also enable study of binary or multiple star systems with characteristic separation of a few to tens of milliarcseconds.

6 OUTLOOK AND DISCUSSION

Here, we have presented a new method to enable a single Cherenkov telescope to operate as an intensity interferometer composed of many individual elements. Ray-tracing simulations using a proposed design of an intensity interferometer system implemented on an IACT indicated the feasibility of the proposed technique. The baselines achievable are far shorter than that between the different telescopes and thus could expand the scientific scope of IACT-SII observatories.

The proposed instrument mitigates several limitations of IACTs when used as intensity interferometers, thus suggesting its possibility as an alternative to current designs of IACT-SII instruments. Its implementation would enable the the characterization of sources over both relatively large and small angular scales, set by the array telescope spacing, and individual telescope sizes, respectively. The subdivision of the pupil provides an improved temporal response, and the collimation enables narrower spectral filtering. Time-tagging individual photon events is possible as the photon count rate in each subdivision becomes much less than the detector or electronic bandwidth, even for relatively bright targets. This greatly simplifies the required data bandwidth and improves the rejection of unwanted spurious correlations. When considering more traditional intensity interferometry targets, which are not partially resolved over the telescope diameter, the segmentation approach offers a natural way to measure the zero-baseline correlation by correlating one-half of the subdivisions with the other half. This zero-baseline correlation provides a model-independent estimation of the squared visibility to ultimately reduce measurement uncertainties on the derived stellar parameters.

A possible addition to the optical system is a mask that partially obscures the light that is concentrated into each detector. An example would be a grid of circular apertures, where each circle is aligned with the concentrating optics/detector centre. At the cost of light throughput, such a system would help provide a cleaner mapping between the rays that originate from a given light collector subregion and the detector. In the tilings considered here, the subregion edges are touching, and even overlapping, and this could be problematic in data reduction and analysis. Using a mask, each subregion is better approximated as a point-like aperture simplifying the data interpretation.

The hexagonal tiling chosen here was inspired by the use of Winston cones used frequently for IACT gamma-ray cameras in conjunction with photomultiplier tubes or, more recently, silicon photomultipliers. Here, we considered a relatively large number of subdivisions however in practice the total number could be reduced

to allow for a simpler implementation. The polar tiling was chosen to minimize the arrival time distribution in any single segment, however, this sort of irregular tiling can likely only be achieved using a large area multipixel camera that can record the position and time of individual photon events to nanosecond or better precision. While such a detector does not commercially exist, one could imagine incorporating the necessary readout electronics into large-area SiPM cameras. This capability to record the arrival time along with the transverse coordinate location of photon events enables the subdivision to be performed entirely in post-processing. The tiling could then be optimized based on the target parameters and instrumental limitations.

ACKNOWLEDGEMENTS

We acknowledge the financial support of the French National Research Agency (ANR, project I2C, ANR-20-CE31-0003). This research has made use of the Jean-Marie Mariotti Center (JMMC) Measured Stellar Diameters Catalogue.[3] The authors would like to thank the Very Energetic Radiation Imaging Array System (VERITAS) collaboration for their communication of relevant information for our simulation studies. Furthermore we would like to thank Tugdual LeBohec and William Guerin for their constructive reviews of the paper.

DATA AVAILABILITY

All simulated data presented in this work are available upon reasonable request. Specific information on the ray-tracing model may require approval from the VERITAS collaboration before release.

REFERENCES

Abe S. et al., 2024, MNRAS, 529, 4387
Abeysekara A. U. et al., 2020, Nat. Astron., 4, 1164
Acciari V. A. et al., 2020, MNRAS, 491, 1540
Acharyya A. et al., 2024, ApJ, 966, 28
Baldwin J. E., Haniff C. A., Mackay C. D., Warner P. J., 1986, Nature, 320, 595
Bessell M. S., 1979, PASP, 91, 589
Born M., Wolf E., 1980, in Born M., Wolf E., eds, Principles of Optics, 6th edn. Pergamon, New York, p. 491, available at : https://doi.org/10.1016/B978-0-08-026482-0.50017-7
Duvert G. 2016 VizieR Online Data Catalog, p. II/345
Challouf M. et al., 2014, A&A, 570, A104
Cortina J. et al., 2022, in Mérand A., Sallum S., Sanchez-Bermudez J., eds, Proc. SPIE Conf. Ser. Vol. 12183, Optical and Infrared Interferometry and Imaging VIII. SPIE, Bellingham, p. 121830C
Davies J. M., Cotton E. S., 1957, Sol. Energy, 1, 16, available at: https://doi.org/10.1016/0038-092X(57)90116-0
de Almeida E. S. G. et al., 2022, MNRAS 55, 1
Donati J. F., Semel M., Carter B. D., Rees D. E., Collier Cameron A., 1997, MNRAS, 291, 658
Dravins D. et al., 2005, in Instrumentation for Extremely Large Telescopes held at Ringberg Castle, Bavaria, 25–29 July 2005. preprint (arXiv:astro-ph/0511027)
Gori P.-M. et al., 2021, MNRAS, 505, 2328
Guerin W., Dussaux A., Fouché M., Labeyrie G., Rivet J.-P., Vernet D., Vakili F., Kaiser R., 2017, MNRAS, 472, 4126
Guerin W., Rivet J.-P., Fouché M., Labeyrie G., Vernet D., Vakili F., Kaiser R., 2018, MNRAS, 480, 245
Hanbury Brown R., 1974, The Intensity Interferometer. Its Applications to Astronomy. Taylor and Francis, Toronto
Hanbury Brown R., Twiss R. G., 1954, Phil. Mag., 45, 663
Hanbury Brown R., Twiss R. Q., 1956, Nature, 177, 27
Hanbury Brown R., Twiss R. Q., 1958, RSPA, 243, 291
Holder J. et al., 2006, Astropart. Phys., 25, 391
Khintchine A., 1934, Math. Ann., 109, 604
Labeyrie A., Lipson S. G., Nisenson P., 2006, An Introduction to Optical Stellar Interferometry. Cambridge Univ. Press, Cambridge
LeBohec S., Holder J., 2006, ApJ, 649, 399
Mandel L., Wolf E., 1995, Optical Coherence and Quantum Optics. Cambridge Univ. Press, Cambridge
Matthews N. et al., 2023, AJ, 165, 117
Monnier J. D., Tuthill P. G., Danchi W. C., 1999, ApJ, 525, L97
Mourard D. et al., 2022, in Mérand A., Sallum S., Sanchez-Bermudez J., eds, Proc. SPIE Conf. Ser. Vol. 12183, Optical and Infrared Interferometry and Imaging VIII. SPIE, Bellingham, p. 1218308
Nardetto N. et al., 2020, A&A, 639, A67
Okumura A., Noda K., Rulten C., 2016, Astropart. Phys., 76, 38
Petit P., Louge T., Théado S., Paletou F., Manset N., Morin J., Marsden S. C., Jeffers S. V., 2014, PASP, 126, 469
Rivet J. P. et al., 2020, MNRAS, 494, 218
Roache E., Irvin R., Perkins J. S., Harris K., Falcone A., Finley J., Weeks T., 2008, Proc. Sci., 37th International Cosmic Ray Conference. SISSA, Trieste, PoS#1397
Rou J., Nuñez P. D., Kieda D., LeBohec S., 2013, MNRAS, 430, 3187
Siegert A. J. F., 1943, On the fluctuations in signals returned by many independently moving scatterers, Report/Radiation Laboratory, Massachusetts Institute of Technology, Vol 465, https://www.tib.eu/de/suchen/id/TIBKAT%3A584715161
Stee P. et al., 2012, A&A, 545, A59
Wentz T., Saha P., 2015, MNRAS, 446, 2065
Wiener N., 1930, Acta Math., 55, 117
Zmija A., Vogel N., Wohlleben F., Anton G., Zink A., Funk S., 2024, MNRAS, 527, 12243

This paper has been typeset from a TEX/LATEX file prepared by the author.

[3]available at http://www.jmmc.fr/jsdc